Title
Modal parameter identification of a MEMS gyroscope

Permalink
https://escholarship.org/uc/item/54k0h6xz

Authors
M'Closkey, RT
Gibson, S
Hui, J

Publication Date
2000

Peer reviewed

Modal Parameter Identification of a MEMS Gyroscope [1]

Robert T. M'Closkey, Steve Gibson, and Jason Hui
Mechanical and Aerospace Engineering Department
University of California, Los Angeles 90095-1597, U.S.A.
rtm@obsidian.seas.ucla.edu, gibson@seas.ucla.edu, huij@seas.ucla.edu

Abstract

This paper reports the experimental system identification of the Jet Propulsion Laboratory MEMS vibrational rate gyroscope. A high-order two-input/two-output transfer function for the microgyroscope is identified and mapped to a three-mode rigid plate model that reveals the orientation of important vibrational modes.

1 Introduction

A new generation of microelectromechanical (MEMS) gyroscopes is being developed at the Jet Propulsion Laboratory for spacecraft applications such as attitude stabilization, maneuver control, and tumble recovery. The advantages of these microsensors over conventional inertial navigation instruments include: 1) compact size and weight savings, 2) low power consumption, and 3) a low cost micromachining process.

For microsensors to realize the performance levels of which they are capable, innovative methods are required for device calibration and active control of sensor dynamics. This paper presents a method for identification of a physical model of a microgyro from input/output data. The physical model, as opposed to an input/output model, reveals the orientation of the two rocking mode axes and distinguishes the rocking modes from the plunging mode of the gyro. Because the microgyros are based on the coriolis-induced coupling between the rocking modes, knowledge of the rocking mode axes' orientations are essential for implementation of control loops and calibration methods that compensate for the devices' sensitivity to operating conditions.

The approach here first uses a fast recursive least-squares algorithm to identify a MIMO transfer function from input/output data. Next, because the coefficients in the identified transfer function are related to the physical parameters in a nonlinear way, we develop an algorithm to extract from the identified transfer function a rigid plate model that captures the three dominant mechanical modes of the gyro.

The identification results demonstrate that the nodal axes of the rocking modes do not necessarily coincide with the symmetry axes of the gyro's sensing and drive components. The axes' orientations are verified independently with measurements from a laser vibrometer, which is not available in microgyro applications.

2 JPL Microgyroscope Operating Principles

The Jet Propulsion Laboratory microgyroscope is a vibrational rate sensor whose operation depends on the coupling of energy in one degree of freedom to another degree of freedom within the sensor. Excitation of the microgyro dynamics is achieved by applying a potential to the two drive electrodes, denoted D_1 and D_2, in Figure 1. The drive electrodes and sense electrodes (denoted S_1 and S_2), are suspended by silicon springs above matching electrodes on the base plate. The large post is rigidly attached to the center of the "cloverleaf" formed by D_1, D_2, S_1 and S_2. The post adds inertia to the system which boosts the sensitivity to rotational motion. The electrical potential between the drive electrodes and their respective base plate electrodes creates an electrostatic force that, ideally, rocks the cloverleaf assembly about the y-axis. The amplitude of the rocking motion can be maximized by driving the electrodes at the natural frequency of this degree of freedom, known as the *drive mode*. If the device is rotated about the z-axis, then the rocking about y is coupled into rocking about the x-axis via coriolis acceleration in the x-y frame fixed to the gyro. The rocking about the x-axis is referred to as the *sense mode* and the x-axis response is related to the angular rate of rotation about z. Further information on the operating principles of the microgyro, fabrication details and preliminary performance results may be found in Tang et al. [4,5,6].
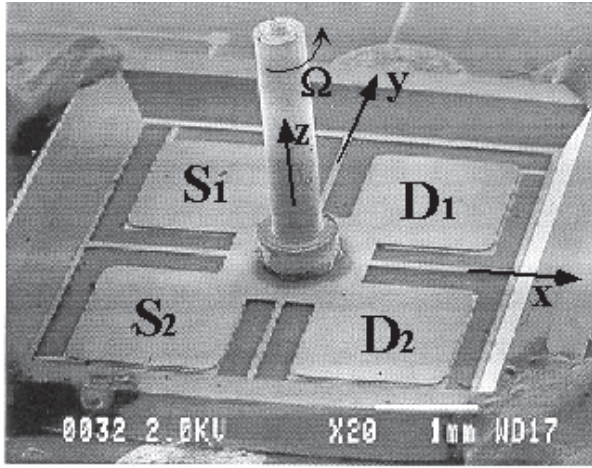
Figure 1: JPL microgyro with sense and actuator electrodes labeled (picture courtesy of T. Tang).

Figure 2: Comparison of 40*th*-order model (solid) and three degree of freedom rigid plate model (dash).

3 Identification of Input/Output Models

3.1 ARX Models

The objective of the identification is to accurately model the dynamic response of the gyroscope as represented by the two-input/two-output transfer function from drives D_1 and D_2 to sensors S_1 and S_2. This transfer function is assumed to have the form of the linear ARX (Auto-Regressive with eXogenous input) model

$$A(z)y = B(z)u, \tag{1}$$

where $A(z)$ and $B(z)$ are matrix polynomials in which the coefficients are 2×2 matrices, and y and u represent the 2×1 measured output sequences and applied input sequences, respectively.

Details of the ARX model identification with an adaptive lattice multichannel lattice filter are presented in [3]. In this paper we describe the choice of test inputs, model order selection, and frequency domain weighting of the prediction error for identification of accurate models. This paper also demonstrates that MIMO experiments and identification must be employed to determine the two very closely spaced rocking modes in the microgyro.

Figure 2 displays the magnitude of the frequency responses of the 40*th*-order two-input/two-output identified model (the dashed plots are explained in Section 4). The transfer functions reveal two modes less than 2 Hz apart near 535 Hz. These modes are the rocking modes of the microgyro. Extracting the modal frequencies from the identified model yields rocking modes at 534.5 Hz and 536.4 Hz. The third prominent mode is the plunging mode, the "axial" degree of freedom in the sensor, and is located at 590.3 Hz. The modal

frequencies determined from the identified model have also been confirmed with a dynamic signal analyzer.

The two rocking modes and plunging mode dominate the frequency response of the gyro so it is useful to consider a six-state approximation of the 40*th*-order model. The six-state approximation is obtained from the truncation of the balanced state-space realization of the 40*th*-order model. Balanced realizations and model reduction are discussed in Green and Limebeer [1] and Zhou et al. [7]. The eight largest Hankel singular values of the 40*th*-order model are

$$\begin{bmatrix} 15.2 & 15.2 & 6.75 & 6.75 & 3.49 & 3.48 & 0.0652 & 0.0651 \end{bmatrix}.$$

Truncating the system to the first six states of the balanced realization results in very small approximation error as is evident from these Hankel singular values. The eigenvalues of this six-state system are three sets of complex conjugate pairs forming a three-mode system approximating the rocking modes and plunging mode of the gyro dynamics.

The transfer function representation for the six-state model is

$$\begin{aligned}
\tilde{H}(s) &= \begin{bmatrix} \tilde{S}_1/D_1 & \tilde{S}_1/D_2 \\ \tilde{S}_2/D_1 & \tilde{S}_2/D_2 \end{bmatrix} \\
&= \frac{1}{d_1} \left(s \begin{bmatrix} 6.067 & -0.9687 \\ -21.06 & 3.649 \end{bmatrix} + \begin{bmatrix} 7063 & -397.6 \\ -54670 & 5861 \end{bmatrix} \right) \\
&+ \frac{1}{d_2} \left(s \begin{bmatrix} -5.423 & -19.02 \\ -1.233 & -4.559 \end{bmatrix} + \begin{bmatrix} -5408 & -50450 \\ -727.3 & -9474 \end{bmatrix} \right) \quad (2) \\
&+ \frac{1}{d_3} \left(s \begin{bmatrix} 21.31 & 21.34 \\ 23.09 & 23.13 \end{bmatrix} + \begin{bmatrix} 64680 & -64740 \\ 69500 & 69570 \end{bmatrix} \right).
\end{aligned}$$

The polynomials d_1, d_2 and d_3 are the two rocking modes and plunging mode dynamics, respectively,

where $d_i(s) = s^2 + 2\zeta_i\omega_i + \omega_i^2$, and

$$\zeta_1 = 3.167 \times 10^{-4}, \quad \omega_1 = 534.5 * 2\pi$$
$$\text{(first rocking mode)}$$
$$\zeta_2 = 1.586 \times 10^{-4}, \quad \omega_2 = 536.4 * 2\pi$$
$$\text{(second rocking mode)} \tag{3}$$
$$\zeta_3 = 11.70 \times 10^{-4}, \quad \omega_3 = 590.3 * 2\pi$$
$$\text{(plunging mode)}.$$

The sense channels in (2) are written $\tilde{S}_i$ to remind us that this truncated model still contains the effects of the anti-aliasing filter dynamics. Without the additional phase lag introduced by the filter one would expect (2) to contain only s terms in the numerator since velocity measurements are used in the gyro. The anti-aliasing filter, however, changes the phase of the electrode measurements and this effect must be removed since Section 4 requires models based only on the gyro dynamics. This is accomplished by approximating each modal contribution in the transfer function (2), on a channel-by-channel basis, with a transfer function based on velocity measurements and explicitly including the anti-aliasing filter G_{aa}. For example, the first rocking mode transfer function excluding the anti-aliasing filter for the S_1/D_1 channel is approximated as $\beta_{111}s/d_1(s)$ where β_{111} is determined from

$$\beta_{111} := \arg\min_{\beta} \left\| \frac{6.067s + 7063}{d_1(s)} - G_{\mathrm{aa}}(s)\frac{\beta s}{d_1(s)} \right\|_{\infty}, \tag{4}$$

where $\|\cdot\|_{\infty}$ is the $\mathcal{H}_{\infty}$ norm. The objective function is convex in β and so a simple bisection routine is used to compute (4). This approximation yields the following transfer function relating the drive inputs to the sense measurements without the anti-aliasing filter dynamics

$$H(s) = \begin{bmatrix} S_1/D_1 & S_1/D_2 \\ S_2/D_1 & S_2/D_2 \end{bmatrix}$$
$$= \frac{s}{d_1(s)} \begin{bmatrix} \beta_{111} & \beta_{121} \\ \beta_{211} & \beta_{221} \end{bmatrix} + \frac{s}{d_2(s)} \begin{bmatrix} \beta_{112} & \beta_{122} \\ \beta_{212} & \beta_{222} \end{bmatrix}$$
$$+ \frac{s}{d_3(s)} \begin{bmatrix} \beta_{113} & \beta_{123} \\ \beta_{213} & \beta_{223} \end{bmatrix}, \tag{5}$$

where

$$\begin{bmatrix} \beta_{111} & \beta_{121} \\ \beta_{211} & \beta_{221} \end{bmatrix} = \begin{bmatrix} 6.240 & -0.8787 \\ -26.52 & 4.014 \end{bmatrix}$$
$$\begin{bmatrix} \beta_{112} & \beta_{122} \\ \beta_{212} & \beta_{222} \end{bmatrix} = \begin{bmatrix} -5.425 & -24.10 \\ 1.153 & -5.355 \end{bmatrix}$$
$$\begin{bmatrix} \beta_{113} & \beta_{123} \\ \beta_{213} & \beta_{223} \end{bmatrix} = \begin{bmatrix} 27.49 & 27.53 \\ 29.70 & 29.74 \end{bmatrix}.$$

A comparison of (5) with the 40*th*-order model is deferred until the next section.

4 Mapping I/O Models to Physical Models

Most system identification methods, including the lattice-filter-based algorithms that we use in Section 3, estimate input/output models. In applications of feedback control, the controller design commonly is based on an identified input/output model or a state-space realization of an identified input/output model. Such realizations are either canonical control or observer forms or balanced realizations, and the mathematical states in these realizations rarely represent physical states. In most control applications, the controllers are designed to drive all states to zero or to regulate particular measured outputs. In either case, the transformation from the mathematical states realized from the identified I/O model to physical states is not needed.

Physical models are system descriptions in which the states represent physical phenomena, such as cloverleaf rocking about a particular axis in the JPL microgyro. Calibration of the JPL microgyro and design of feedback compensation requires not only the identification of input/output models, but also mapping the identified I/O model to a physical model that captures key physical states and parameters internal to the sensor.

The objective is to recover the rocking mode axes from analysis of the input/output model so that the drive and sense axes can be distinguished in the cloverleaf plane, about which the cloverleaf rocks, or the angular velocity of the sensor cannot be inferred from the sense electrode measurements. This can be accomplished only if additional structure is imposed on the identification problem. Specifically, since the two rocking modes and plunging mode dominate the frequency response we introduce a simple rigid plate model with three degrees of freedom to capture these modes. This is what we designate as a "physical" model because we assign physical significance to the states of a certain coordinate representation of the model.

The top view of the rigid plate model in Figure 3 shows the parameters we use to define the perpendicular distance from the (unknown) location of the sense and actuator electrode *centroids* to the rocking mode axes. The plunging mode corresponds to the plate model moving in and out of the plane of the page in Figure 3. Although the sense and drive electrodes make measurements and apply forces distributed over the electrode surface, we can conceptually think of a location on the electrode surface —the centroid —where an equivalent velocity is measured or force is applied. The participation of a particular rocking mode in the transfer function is determined by various products of these parameters: the authority over a given rocking mode by a point force acting at the drive centroid is proportional to the perpendicular distance from the drive centroid to the rocking axis associated with that mode; simi-

larly, the velocity at the sense centroid due to a particular mode is proportional to the perpendicular distance from its rocking axis to the sense centroid. The distances from the sense centroids to the lower frequency rocking mode axis (respectively, higher frequency rocking mode axis) are denoted ξ_{11} and ξ_{21} (respectively, ξ_{12} and ξ_{22}). The distances from the drive centroids to the axis of the lower frequency rocking mode (respectively, higher frequency rocking mode) are denoted η_{11} and η_{21} (respectively, η_{12} and η_{22}). These parameters are labeled in Figure 3.

The ξ's and η's relate how point forces and point velocity measurements affect, and are affected by, the position of the centroids relative to the rocking mode axes. A complete model, however, must include extra degrees of freedom that reflect the *gains* of sense and drive electrodes. The forces applied at the drive electrodes' centroids are "converted" from the electrical potentials specified by the D/A boards. The same analogy can be made for the sense electrodes: the measured sense voltages are converted from the velocity of the sense electrodes' centroids. These conversion factors are constant gains associated with the drive and sense electrodes. This view is especially motivated for the sense electrodes since (nonidentical) transimpedance amplifiers are used to convert a capacitance change into a voltage proportional to the electrode's velocity. We denote the electrode gains associated with S_1 and S_2 as K_{S_1} and K_{S_2}, respectively. The electrode gains associated with D_1 and D_2 are denoted K_{D_1} and K_{D_2}, respectively.

The state-space model of the rocking modes with these parameters is

$$\begin{bmatrix} \dot{x}_1 \\ \dot{x}_2 \end{bmatrix} = \begin{bmatrix} 0 & 1 \\ -\omega_j^2 & -2\zeta_j\omega_j \end{bmatrix} \begin{bmatrix} x_1 \\ x_2 \end{bmatrix}$$
$$+ \begin{bmatrix} 0 & 0 \\ \eta_{1j} & \eta_{2j} \end{bmatrix} \begin{bmatrix} K_{D_1} & 0 \\ 0 & K_{D_2} \end{bmatrix} \begin{bmatrix} D_1 \\ D_2 \end{bmatrix} \qquad j=1,2,$$
$$\begin{bmatrix} S_1 \\ S_2 \end{bmatrix} = \begin{bmatrix} K_{S_1} & 0 \\ 0 & K_{S_2} \end{bmatrix} \begin{bmatrix} 0 & \xi_{1j} \\ 0 & \xi_{2j} \end{bmatrix} \begin{bmatrix} x_1 \\ x_2 \end{bmatrix}, \tag{6}$$

where ζ_j and ω_j, $j=1,2$, are the damping ratios and frequencies associated with the rocking modes (cf. (3)). Thus, this model represents each rocking mode as a damped harmonic oscillator with velocity outputs. A calculation reveals that the transfer function specified by (6) is

$$\frac{s}{d_j(s)} \begin{bmatrix} K_{S_1} & 0 \\ 0 & K_{S_2} \end{bmatrix} \begin{bmatrix} \xi_{1j} \\ \xi_{2j} \end{bmatrix} \begin{bmatrix} \eta_{1j} & \eta_{2j} \end{bmatrix} \begin{bmatrix} K_{D_1} & 0 \\ 0 & K_{D_2} \end{bmatrix},$$
where
$$d_j(s) = s^2 + 2\zeta_j\omega_j s + \omega_j^2.$$

The plunging mode is treated in a similar manner with the exception that forces at each drive electrode iden-
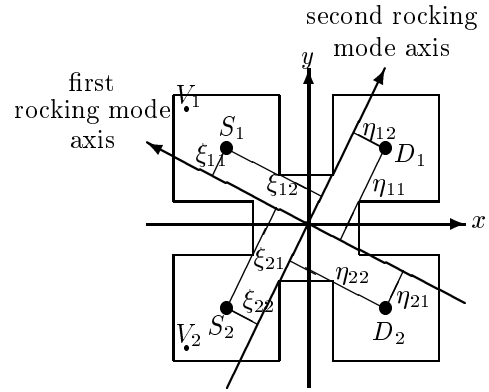
Figure 3: Rigid plate model for the two rocking modes and plunging mode.

tically affects the plunging mode. The velocities measured at the sense electrodes are also the same since the plate model is *translating* as a rigid body for the plunging mode. The unknown parameters that specify the effect of forces applied to, and velocity measurements made from, the plunging mode are denoted α_D, and α_S, respectively. This produces the following plunging mode equations

$$\begin{bmatrix} \dot{x}_1 \\ \dot{x}_2 \end{bmatrix} = \begin{bmatrix} 0 & 1 \\ -\omega_3^2 & -2\zeta_3\omega_3 \end{bmatrix} \begin{bmatrix} x_1 \\ x_2 \end{bmatrix}$$
$$+ \begin{bmatrix} 0 & 0 \\ \alpha_D & \alpha_D \end{bmatrix} \begin{bmatrix} K_{D_1} & 0 \\ 0 & K_{D_2} \end{bmatrix} \begin{bmatrix} D_1 \\ D_2 \end{bmatrix}$$
$$\begin{bmatrix} S_1 \\ S_2 \end{bmatrix} = \begin{bmatrix} K_{S_1} & 0 \\ 0 & K_{S_2} \end{bmatrix} \begin{bmatrix} 0 & \alpha_S \\ 0 & \alpha_S \end{bmatrix} \begin{bmatrix} x_1 \\ x_2 \end{bmatrix} \tag{7}$$
$$\implies \frac{s}{d_3(s)} \alpha_S \alpha_D \begin{bmatrix} K_{S_1} \\ K_{S_2} \end{bmatrix} \begin{bmatrix} K_{D_1} & K_{D_2} \end{bmatrix}.$$

Linear superposition allows us to combine the three transfer functions comprising the rigid plate model into one transfer function that describes the input/output behavior of the plate. The final transfer function is the sum of the individual transfer functions for each mode.

The ξ's, η's, $K_{S_1}, \ldots, K_{D_2}$, and α_S and α_D can be computed by comparing (5) to the rigid plate transfer function and produces the following algebraic equations

$$\begin{bmatrix} K_{S_1}\xi_{11} \\ K_{S_2}\xi_{21} \end{bmatrix} \begin{bmatrix} K_{D_1}\eta_{11} & K_{D_2}\eta_{21} \end{bmatrix} = \underbrace{\begin{bmatrix} \beta_{111} & \beta_{121} \\ \beta_{211} & \beta_{221} \end{bmatrix}}_{M_1} \tag{8}$$

$$\begin{bmatrix} K_{S_1}\xi_{12} \\ K_{S_2}\xi_{22} \end{bmatrix} \begin{bmatrix} K_{D_1}\eta_{12} & K_{D_2}\eta_{22} \end{bmatrix} = \underbrace{\begin{bmatrix} \beta_{112} & \beta_{122} \\ \beta_{212} & \beta_{222} \end{bmatrix}}_{M_2} \tag{9}$$

$$\alpha_S \alpha_D \begin{bmatrix} K_{S_1} \\ K_{S_2} \end{bmatrix} \begin{bmatrix} K_{D_1} & K_{D_2} \end{bmatrix} = \underbrace{\begin{bmatrix} \beta_{113} & \beta_{123} \\ \beta_{213} & \beta_{223} \end{bmatrix}}_{M_3} \tag{10}$$

Solving these equations allows us to interpret the microgyro dynamics in terms of a three-mode rigid plate model. The matrices formed from the plate parameters on the left hand side of the equalities in (8)–(10) are rank one and the singular value decomposition (SVD) will be used to approximate the data matrices with the nearest, in the sense of the matrix 2-norm, rank one matrix. The SVD of M_3 is

$$M_3 = \begin{bmatrix} 0.6793 & 0.7338 \\ 0.7338 & -0.6793 \end{bmatrix} \cdot \begin{bmatrix} 57.27 & 0 \\ 0 & 1.370 \times 10^{-5} \end{bmatrix}$$
$$\cdot \begin{bmatrix} 0.7066 & 0.7076 \\ 0.7076 & -0.7066 \end{bmatrix}^T.$$

The rank one approximation of M_3 is

$$M_3 \approx 57.27 \begin{bmatrix} 0.6793 \\ 0.7338 \end{bmatrix} \begin{bmatrix} 0.7066 & 0.7076 \end{bmatrix}$$

and so the sense electrode and drive electrode gains are computed to be

$$\begin{bmatrix} K_{S_1} \\ K_{S_2} \end{bmatrix} = \nu_S \begin{bmatrix} 0.6793 \\ 0.7338 \end{bmatrix} \qquad \begin{bmatrix} K_{D_1} \\ K_{D_2} \end{bmatrix} = \nu_D \begin{bmatrix} 0.7066 \\ 0.7066 \end{bmatrix},$$

The constants ν_S and ν_D reflect the fact that we cannot uniquely determine α_S and α_D, and hence K_{S_1}, K_{S_2}, K_{D_1}, and K_{D_2}, without additional information. In the sequel we will be concerned with the *ratios* of the ξ's and η's so any common factor between elements in a given vector does not change the result. Thus we set $\nu_S = \nu_D = 1$ without loss of generality. Note that M_3 is almost rank one since the condition number of M_3 is greater than 4×10^6. This analysis also indicates an imbalance between the sense electrode gains K_{S_2} and K_{S_2} of about 8%.

Estimates of ξ's and η's are obtained from computing SVDs of M_1 and M_2 after pre- and post-multiplication by the electrode gain matrices

$$\begin{bmatrix} K_{S_1} & 0 \\ 0 & K_{S_2} \end{bmatrix}^{-1} M_1 \begin{bmatrix} K_{D_1} & 0 \\ 0 & K_{D_2} \end{bmatrix}^{-1}$$
$$= \begin{bmatrix} 0.2460 & -0.9693 \\ -0.9693 & -0.2460 \end{bmatrix} \cdot \begin{bmatrix} 53.36 & 0 \\ 0 & 0.1312 \end{bmatrix} \cdot$$
$$\begin{bmatrix} 0.9889 & -0.1488 \\ -0.1488 & -0.9888 \end{bmatrix}^T,$$
$$\begin{bmatrix} K_{S_1} & 0 \\ 0 & K_{S_2} \end{bmatrix}^{-1} M_2 \begin{bmatrix} K_{D_1} & 0 \\ 0 & K_{D_2} \end{bmatrix}^{-1} \qquad (11)$$
$$= \begin{bmatrix} -0.9796 & 0.2011 \\ -0.2011 & -0.9796 \end{bmatrix} \cdot \begin{bmatrix} 52.46 & 0 \\ 0 & 0.09799 \end{bmatrix} \cdot$$
$$\begin{bmatrix} 0.2196 & -0.9756 \\ 0.9756 & 0.2196 \end{bmatrix}^T.$$

The condition numbers of these matrices are greater than 400 and so they are accurately approximated by

rank one matrices from which the parameter estimates are extracted. The ξ's and η's are determined, within a multiplicative factor, to be

$$\begin{bmatrix} \xi_{11} \\ \xi_{21} \end{bmatrix} \propto \begin{bmatrix} 0.2460 \\ -0.9693 \end{bmatrix}, \qquad \begin{bmatrix} \eta_{11} \\ \eta_{21} \end{bmatrix} \propto \begin{bmatrix} 0.9889 \\ -0.1488 \end{bmatrix},$$
$$\begin{bmatrix} \xi_{12} \\ \xi_{22} \end{bmatrix} \propto \begin{bmatrix} -0.9796 \\ -0.2011 \end{bmatrix}, \qquad \begin{bmatrix} \eta_{12} \\ \eta_{22} \end{bmatrix} \propto \begin{bmatrix} 0.2196 \\ 0.9756 \end{bmatrix}. \qquad (12)$$

The data from the identified model (5) conforms to the properties of the rigid plate model (i.e., M_i are essentially rank one matrices) and gives us confidence in the rigid plate model as a suitable representation of the gyro dynamics.

A comparison of the plate model and the 40*th*-order identified model is made in Figure 2. The frequency response of the three-mode rigid plate model is an excellent approximation to the full-order identified model.

4.1 Rocking Mode Axis Orientation from the Rigid Plate Model
Locating the rocking mode axes with respect to the sensor's frame, or equivalently the x–y axes in Figure 1, requires that we determine or assume the position of the electrode centroids. We proceed by assuming that the sense centroids are located in the center of the sense electrodes versus assuming the drive centroids are located in the center of the drive electrodes. The results of this comparison are also contrasted to displacement measurements made with a laser vibrometer.

Figure 3 shows the variables used in orienting the rocking mode axes with respect to the x–y frame *assuming* the sense centroids are located in the middle of the electrode and the rocking mode axes pass through the geometric center of the gyro. These assumptions imply that the angle subtended from one centroid to the origin of the x–y axes to the other centroid is 90 degrees. In this case, the angles θ_1 and θ_2 are the angles between the negative x-axis and the first rocking mode axis (in a counterclockwise sense) and the second rocking mode axis, respectively, and are calculated to be

$$\theta_{1,S} = \tan^{-1}\left(1 - \frac{2|\xi_{21}|}{|\xi_{11}| + |\xi_{21}|}\right) = 30.8°$$
$$\theta_{2,S} = 45° + \tan^{-1}\left(\left|\frac{\xi_{12}}{\xi_{22}}\right|\right) = 123°. \qquad (13)$$

Alternatively, using the drive parameters gives

$$\theta_{1,D} = \tan^{-1}\left(1 - \frac{2|\eta_{11}|}{|\eta_{21}| + |\eta_{11}|}\right) = 36.4°$$
$$\theta_{2,D} = 45° + \tan^{-1}\left(\left|\frac{\eta_{22}}{\eta_{12}}\right|\right) = 122°. \qquad (14)$$

Note that only the ratios of ξ's or η's, appearing in the same vectors in (12), are required in these calculations thereby verifying our assertion that multiplicative constants in the parameters do not affect the analysis.

The orientation estimates for the second rocking mode axis are very close, and the estimates for the first rocking mode axis differ by about six degrees. The axes' orientations from vibrometer data are obtained by analyzing identified models with the vibrometer displacement measurements. The locations of the laser spots are shown in Figure 3 as V_1 and V_2. Using a procedure entirely analogous to the sense electrode measurement case, the identified models using the vibrometer measurements are balanced, truncated, and phase corrected, yielding the following independent estimates of the node orientation

$$\tilde{\theta}_1 = 33.4^\circ, \qquad \tilde{\theta}_2 = 130^\circ.$$

Thus, $\tilde{\theta}_1$ is within 3 degrees of the estimates from (13), and $\tilde{\theta}_2$ is within 8 degrees of the estimates from (14). The vibrometer estimates are reliable but they do contain the effects of positioning errors which are difficult to quantify since the laser spot is positioned by eye on the mechanical structure of the gyro.

5 Conclusion

This paper addresses system identification and model development for the Jet Propulsion Laboratory microgyroscope. High-order, multi-input/multi-output linear models are required to capture important characteristics of the gyro dynamics such as closely spaced modal frequencies. Frequency response plots show that the three key modes corresponding to the sensor's two rocking modes and plunging mode are well-modeled with the six-state approximation of the high-order model.

The orientation of the rocking mode axes with respect to the sense and drive electrodes is also determined. This information is not immediately available from the identified input/output model. A physical model of gyro, specified as an elastically suspended rigid plate with three degrees of freedom (representing the two rocking modes and plunging mode), is introduced to extract the rocking mode axes orientations from the identified model. Our results show that the rocking mode axes are not necessarily aligned with the convenient sense/drive electrode coordinate frame.

References:

1. Green, M., and Limebeer, D., *Linear Robust Control*, Prentice-Hall, New Jersey, 1995.

2. Jiang, S.-B., and Gibson, J.S., "An unwindowed multichannel lattice filter with orthogonal channels," *IEEE Trans. Signal Processing*, v. 43, no. 12, pp. 2831-2842, December 1995.

3. M'Closkey, R.T., Gibson, J.S., and Hui, J., "Input-Output Dynamics of the JPL Microgyroscope," *37th IEEE Conference on Decision and Control*, December 1998, pp. 4328–4333.

4. Tang, T.K., Gutierrez, R.C., Wilcox, J.Z., Stell, C., Voperian, V., Calvet, R., Li, W., Charkaborty, I., and Bartman, R., "Silicon Bulk Micromachined Vibratory Gyroscope." *Solid-State Sensor and Actuator Workshop*, Hilton Head, South Carolina, 1996.

5. Tang, T.K., Gutierrez, R.C., Wilcox, J.Z., Stell, C.,and others, "Silicon bulk micromachined vibratory gyroscope for microspacecraft." in *Proc. SPIE*, vol.2810:101-15, 1996.

6. Tang, T.K., Gutierrez, R.C., Stell, C.B., Vorperian, V. and others, "A packaged silicon MEMS vibratory gyroscope for microspacecraft." *Tenth Ann. Int. Workshop MEMS*, Nagoya, Japan, pp. 500-5, 1997.

7. Zhou, K., Doyle, J., and Glover, K., *Robust and Optimal Control*, Prentice Hall, New Jersey, 1996.